PHYSICAL REVIEW B **107**, 035419 (2023)

Time evolution of Majorana corner modes in a Floquet second-order topological superconductor

Arnob Kumar Ghosh,[1,2,*] Tanay Nag,[3,†] and Arijit Saha[1,2,‡]
[1]*Institute of Physics, Sachivalaya Marg, Bhubaneswar-751005, India*
[2]*Homi Bhabha National Institute, Training School Complex, Anushakti Nagar, Mumbai 400094, India*
[3]*Department of Physics and Astronomy, Uppsala University, Box 516, 75120 Uppsala, Sweden*

(Received 15 August 2022; revised 9 January 2023; accepted 12 January 2023; published 19 January 2023)

We propose a practically feasible time-periodic sinusoidal drive protocol in an on-site mass term to generate the two-dimensional (2D) Floquet second-order topological superconductor, hosting both the regular 0- and anomalous π-Majorana corner modes (MCMs) while starting from a static 2D topological insulator/d-wave superconductor heterostructure setup. We theoretically study the local density spectra and the time dynamics of MCMs in the presence of such drive. The dynamical MCMs are topologically characterized by employing the average quadrupolar motion. Furthermore, we employ the Floquet perturbation theory (FPT) in the strong driving amplitude limit to provide analytical insight into the problem. We compare our exact (numerical) and the FPT results in terms of the eigenvalue spectra and the time dynamics of the MCMs. We emphasize that the agreement between the exact numerical and the FPT results is more prominent in the higher-frequency regime for close to the zero-quasienergy mode.

DOI: 10.1103/PhysRevB.107.035419

I. INTRODUCTION

The quest for first-order topological superconductors (TSCs) has been engaging substantial attention among the quantum condensed-matter physics community for the past two decades. These TSCs have become the breeding ground for realizing the Majorana zero modes (MZMs) [1–3]. These MZMs are predicted to be associated with a one-dimensional (1D) spinless p-wave superconductor, as proposed by Kitaev [1]. From the practical perspective, they can also be perceived in a heterostructure setup consisting of a 1D Rashba nanowire with strong spin-orbit coupling (SOC) and proximity coupled to an s-wave superconductor [4–6]. Interestingly, such MZMs follow non-Abelian statistics, owing to their nonlocal properties, and can be the building blocks for fault-tolerant quantum computers [7–10]. The hunt for the MZMs is not limited to the theoretical proposals only and there have been a few experimental advancements [11–18] in this direction. However, a distinct signature of the MZMs is yet to be discovered. Moving our attention towards the paradigm of higher-order topological insulators (HOTIs) [19–33] and their superconducting counterparts, i.e., higher-order topological superconductors (HOTSCs) [34–62], they are characterized by the presence of $(d-n)$-dimensional electronic (Majorana) boundary modes, with d the dimension of the system and n $(d \geqslant n \geqslant 2)$ the order of the topological system. There have been a few concurrent experimental developments to realize the HOTI phase in solid-state systems [63,64], phononic crystals [65], acoustic systems [66–68], electric-circuit setups [69], photonic lattice [70,71], etc.

On the other hand, the realm of nonequilibrium systems involving Floquet generation of topological bands provides us with the on-demand control of the topological properties of a system [72–83]. Floquet engineering enables one to achieve a topological phase from a topologically trivial system. In a driven system, one can realize the regular zero mode as well as the so-called anomalous π modes, which do not have any static analog. The latter have been proposed to exist in the first-order Floquet topological systems [74–76,78,79]. A few experimental proposals also come up with brisk theoretical developments [84–89]. Very recently, the concept of Floquet engineering has been extended to generate the Floquet HOTI (FHOTI) [90–109] and the Floquet HOTSC (FHOTSC) [110–116]. The FHOTI has been experimentally contextualized in a metamaterial platform, specifically in the acoustic system in Ref. [117]. However, a real material-based experiment to realize the FHOTI/FHOTSC phase has not been reported so far, to the best of our knowledge.

In the current literature, there exist a few proposals that rely on the periodic kick or step-drive protocol to realize the FHOTI and FHOTSC phases hosting only the zero modes [91,93,99,101,113,114], as well as both the regular zero mode and anomalous π modes [90,94,96,97, 103–106,116]. A handful of schemes exists to generate the FHOTI or FHOTSC phase using a periodic sinusoidal (harmonic) driving protocol [92,102,110,112,115] and periodic laser irradiation [95,100,109]. The previous studies emphasized the generation of both the regular zero mode and anomalous π modes in the FHOTI/FHOTSC phase that are primarily based on sinusoidal temporal variation of the hoppings [92,102,112,115]. In Ref. [110], an oscillating magnetic field is considered to capture the FHOTI phase; however, the

---

[*] arnob@iopb.res.in
[†] tanay.nag@physics.uu.se
[‡] arijit@iopb.res.in

2469-9950/2023/107(3)/035419(12)

©2023 American Physical Society

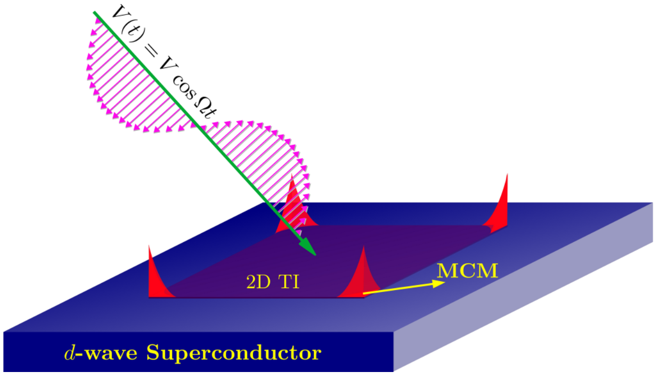

FIG. 1. We depict the schematic representation of our setup, which consists of a two-dimensional (2D) topological insulator (TI) in proximity to a d-wave superconductor while an external time-dependent periodic potential is harmonically driving the system to realize the 0 and π-Floquet Majorana corner modes (MCMs).

anomalous π mode has not been investigated in this model. On the other hand, the periodic sinusoidal/laser irradiation-mediated FHOTI/FHOTSC phase, hosting both the zero and π modes, is technically not as straightforward as the periodic step/kick drive. Due to the continuous time-sequence nature of the above protocols, one cannot obtain the Floquet operator in a closed analytical form. Finding the parameter space where one can realize the anomalous modes is thus cumbersome. In recent times, a few reports have been put forward where a perturbative scheme based on the Floquet perturbation theory (FPT) has been employed to study a driven system in the strong driving limit [118–120]. Following this background, we pose the following intriguing questions: (1) How can one engineer the two-dimensional (2D) Floquet second-order topological superconductor (FSOTSC) hosting both 0- and π-Majorana corner modes (MCMs) employing a periodically varying on-site mass term that can be practically more feasible? (2) How do these MCMs evolve with time? (3) How can one topologically characterize these modes using a proper dynamical invariant? (4) Can the numerical results, in the strong driving limit, be understood using the analytical FPT approach? Here, we intend to investigate these interesting questions that have been unanswered so far.

In this article, we begin with a 2D topological insulator (TI) and d-wave superconductor heterostructure to generate the 2D FSOTSC hosting 0- and π-MCMs using a harmonic drive in the on-site mass term (see Fig. 1). The signature of the MCMs is demonstrated in the local density of states (LDOS) behavior (see Fig. 2). Furthermore, the time evolution of the MCMs is investigated where the zero and π modes emerge even before the full time period (see Fig. 3). We topologically characterize the dynamical system using the average quadrupolar motion (see Fig. 4). Afterward, we make use of the FPT to derive an effective Hamiltonian picture for the system in the strong driving amplitude limit (see Fig. 5). We study the time dynamics of the 0-MCMs for the exact and perturbative time-evolution operator and present a comparison between those two results in the strong driving amplitude limit (see Fig. 6).

The remainder of the article is arranged as follows. We introduce our model Hamiltonian, the driving protocol, and the formalism in Sec. II. The numerical results obtained using the Floquet operator are discussed in Sec. III. We topologically characterize the dynamical 0- and π-MCMs in Sec. IV with an appropriate topological invariant. Section V is devoted to the discussion of the analytical results obtained from the FPT and its comparison with the exact (numerical) results. In Sec. VI, we discuss some relevant points related to our results with their outlooks. Finally, we summarize and conclude our article in Sec. VII.

II. MODEL AND METHOD

In this section, we introduce our model Hamiltonian, driving protocol, and the formalism used to deal with the dynamical problem.

A. Model Hamiltonian

We consider a system consisting of a 2D TI in proximity to a d-wave superconductor (see Fig. 1 for a schematic representation). The system can be described via the following Hamiltonian, written in the Bogoliubov–de Gennes (BdG) form as [37,114]

$$H(\mathbf{k}) = 2\lambda\sin k_x\Gamma_1 + 2\lambda\sin k_y\Gamma_2 + \epsilon(\mathbf{k})\Gamma_3 + \Delta(\cos k_x - \cos k_y)\Gamma_4, \tag{1}$$

where $\epsilon(\mathbf{k}) = (m_0 - 4\gamma + 2\gamma\cos k_x + 2\gamma\cos k_y)$, the hopping (SOC) strength is denoted by γ (λ), and m_0 and Δ stand for the on-site crystal field splitting and d-wave superconducting pairing amplitude (assumed to be induced via the proximity effect), respectively. For static systems, such mean-field d-wave pairing has been theoretically considered before in Refs. [36,37] assuming the proximity effect. The 8×8 $\mathbf{\Gamma}$ matrices are given by $\Gamma_1 = \tau_z\sigma_z s_x$, $\Gamma_2 = \tau_z\sigma_0 s_y$, $\Gamma_3 = \tau_z\sigma_z s_0$, and $\Gamma_4 = \tau_x\sigma_0 s_0$. The Pauli matrices $\boldsymbol{\tau}$, $\boldsymbol{\sigma}$, and $\mathbf{s}$ operate on particle-hole (e, h), orbital $(\tilde{\alpha}, \tilde{\beta})$, and spin $(\uparrow, \downarrow)$ degrees of freedom, respectively. The Hamiltonian [Eq. (1)] is invariant under time-reversal symmetry, $\mathcal{T}^{-1}H(\mathbf{k})\mathcal{T} = H(-\mathbf{k})$, and particle-hole symmetry, $\mathcal{C}^{-1}H(\mathbf{k})\mathcal{C} = -H(-\mathbf{k})$, where $\mathcal{T} = i\tau_0\sigma_0 s_y\mathcal{K}$ and $\mathcal{C} = \tau_y\sigma_0 s_y\mathcal{K}$, with $\mathcal{K}$ representing the complex-conjugation operator. Apart from these discrete symmetries, $H(\mathbf{k})$ also respect the following spatial symmetries: mirror symmetry along x with $\mathcal{M}_x = \tau_x\sigma_x s_0$: $\mathcal{M}_x H(k_x, k_y)\mathcal{M}_x^{-1} = H(-k_x, k_y)$, mirror symmetry along y with $\mathcal{M}_y = \tau_x\sigma_y s_0$: $\mathcal{M}_y H(k_x, k_y)\mathcal{M}_y^{-1} = H(k_x, -k_y)$, fourfold rotation with $C_4 = \tau_z e^{-\frac{i\pi}{4}\sigma_z s_z}$: $C_4 H(k_x, k_y)C_4^{-1} = H(-k_y, k_x)$, mirror rotation-I with $\mathcal{M}_{xy} = C_4\mathcal{M}_y$: $\mathcal{M}_{xy}H(k_x, k_y)\mathcal{M}_{xy}^{-1} = H(k_y, k_x)$, and mirror rotation-II with $\mathcal{M}_{x\bar{y}} = C_4\mathcal{M}_x$: $\mathcal{M}_{x\bar{y}}H(k_x, k_y)\mathcal{M}_{x\bar{y}}^{-1} = H(-k_y, -k_x)$ [62]. These symmetries play a pivotal role in the generation of FHOTSC, a phase which we discuss later in Sec. VI B. The static Hamiltonian $H(\mathbf{k})$ manifests the second-order TSC phase hosting two MZMs per corner when $0 < m_0 < 8\gamma$ and $\Delta \neq 0$ [37,114].

B. Driving protocol and formalism

We consider the following time-dependent harmonic drive [121] (see Fig. 1) in the on-site mass term on top of the static Hamiltonian $H(\mathbf{k})$ [Eq. (1)] to realize the 2D FSOTSC as follows:

$$V(t) = V\cos(\Omega t)\Gamma_3, \tag{2}$$

where V represents the strength of the drive and $\Omega = (2\pi/T)$ is the frequency (time period) of the drive. It is evident that $V(t)$ satisfies $V(t+T) = V(t)$. Hence, the full Hamiltonian $\mathcal{H}(\mathbf{k}, t) = H(\mathbf{k}) + V(t)$ is also time periodic, i.e., $\mathcal{H}(\mathbf{k}, t+T) = \mathcal{H}(\mathbf{k}, t)$. The Fourier components of $\mathcal{H}(\mathbf{k}, t)$ read as

$$\mathcal{H}_\alpha = \int_0^T \frac{dt}{T}\mathcal{H}(\mathbf{k}, t)\, e^{i\alpha\Omega t}. \tag{3}$$

Exploiting the frequency-zone scheme, one can construct the infinite-dimensional time-independent Floquet Hamiltonian as [77]

$$H_F^\infty(\mathbf{k}) = \begin{pmatrix} \ddots & & & \vdots & & & \iddots & & & \\ & \mathcal{H}_{-2} & \mathcal{H}_{-1} & H(\mathbf{k}) - 2\Omega & \mathcal{H}_1 & \mathcal{H}_2 & & & & \\ & & \mathcal{H}_{-2} & \mathcal{H}_{-1} & H(\mathbf{k}) - \Omega & \mathcal{H}_1 & \mathcal{H}_2 & & & \\ & & & \mathcal{H}_{-2} & \mathcal{H}_{-1} & H(\mathbf{k}) & \mathcal{H}_1 & \mathcal{H}_2 & & \\ & & & & \mathcal{H}_{-2} & \mathcal{H}_{-1} & H(\mathbf{k}) + \Omega & \mathcal{H}_1 & \mathcal{H}_2 & \\ & & & & & \mathcal{H}_{-2} & \mathcal{H}_{-1} & H(\mathbf{k}) + 2\Omega & \mathcal{H}_1 & \mathcal{H}_2 \\ & & & & \iddots & & & \vdots & & \ddots \end{pmatrix}. \tag{4}$$

However, the Fourier components $\mathcal{H}_\alpha$ having $|\alpha| > 1$ vanish akin to the mathematical form of the drive. Here, the size of the Hamiltonian $H_F^\infty(\mathbf{k})$ acts as the bottleneck in the numerical studies, especially when either the frequency of the drive is comparable to (or less than) the bandwidth of the system or the drive encompasses higher harmonics of the sinusoidal function in Eq. (2). In such cases, we need to incorporate more Fourier components $\mathcal{H}_\alpha$, which in turn enlarge the size of $H_F^\infty(\mathbf{k})$. To circumvent this issue, we employ the time-domain formalism and use the time-evolution operator $U(\mathbf{k}; t, 0)$ defined in terms of a time-ordered (TO) notation as follows:

$$\begin{aligned} U(\mathbf{k}; t, 0) &= \text{TO}\ \exp\left[-i\int_0^t dt'\mathcal{H}(\mathbf{k}, t')\right] \\ &= \prod_{j=0}^{N-1} U(\mathbf{k}; t_j + \delta t, t_j), \end{aligned} \tag{5}$$

where $U(\mathbf{k}; t_j + \delta t, t_j) = e^{-i\mathcal{H}(\mathbf{k}, t_j)\delta t}$, with $\delta t = \frac{t}{N}$ and $t_j = j\delta t$. However, $U(\mathbf{k}; t_j + \delta t, t_j)$ can be calculated more efficiently using the second-order Trotter-Suzuki formalism as follows [122–125]:

$$U(\mathbf{k}; t_j + \delta t, t_j) = e^{-i\frac{\delta t}{2}V(t_j + \frac{\delta t}{2})}e^{-i\delta t H(\mathbf{k})}e^{-i\frac{\delta t}{2}V(t_j + \frac{\delta t}{2})}. \tag{6}$$

Note that we need to calculate $e^{-i\delta t H(\mathbf{k})}$ only once due to its time-independent nature. We choose the time increment δt in such a way that $U(\mathbf{k}; t, 0)$ always remains unitary. Following Eq. (5), we can construct the Floquet operator $U(\mathbf{k}; T, 0)$ by replacing $t \to T$, which in turn allows us to calculate the eigenvalue spectra and the LDOS therein. This $U(\mathbf{k}; t, 0)$ also facilitate the calculation of topological invariants, which we discuss in the forthcoming section. Following this periodic driving protocol [Eq. (2)], one can generate the 0- and π-MCMs depending upon the choice of the parameter space, which we present in the next section.

III. GENERATION OF ANOMALOUS MCMs AND THEIR TIME DYNAMICS

In this section, we provide all the numerical results obtained using the Floquet operator and the time-evolution operator discussed before.

A. Generation of anomalous MCMs

As discussed earlier, we can obtain the Floquet operator $U(\mathbf{k}; T, 0)$ adopting Eq. (5). We diagonalize the Floquet operator employing open boundary conditions (OBCs) in both directions to acquire the eigenvalue spectra and signature of the localized boundary modes, i.e., the MCMs therein. First, we consider that the system lies in the nontopological regime ($m_0 = -1$) and then we harmonically drive the system to achieve the anomalous π-MCMs. We demonstrate the quasienergy spectra as a function of the state index m in Fig. 2(a), and the presence of the π-MCMs can be distinctly identified from the inset. The corresponding LDOS is shown in Fig. 2(c). Thus, it is evident that the π-MCMs are located at the corners of the system. However, one can also presume the static system to be in the topological regime ($m_0 = 1$), hosting the static MZMs, and the effect of the harmonic drive can be investigated there. We depict the quasienergy spectra for one such scenario in Fig. 2(b). The driven system allows the realization of both the regular 0-MCMs and the anomalous π-MCMs; the latter does not have any static analog and can only be realized in a dynamical system. From the insets, one can identify the presence of both of these modes. The LDOS distribution for the 0- and π-MCMs is qualitatively the same as shown in Fig. 2(c). It is worth mentioning that the generation of the 0- and π-MCMs is not limited to the specific choices of parameter sets and sustains for a considerable range in the parameter space. Nevertheless, we discuss the recipe to generate the FSOTSC in Sec. VI.

B. Time dynamics of the MCMs

While exploring the time evolution of the Floquet modes, we observe that the MCMs are not generated only after the full-time period T; rather, they start appearing after a cer-

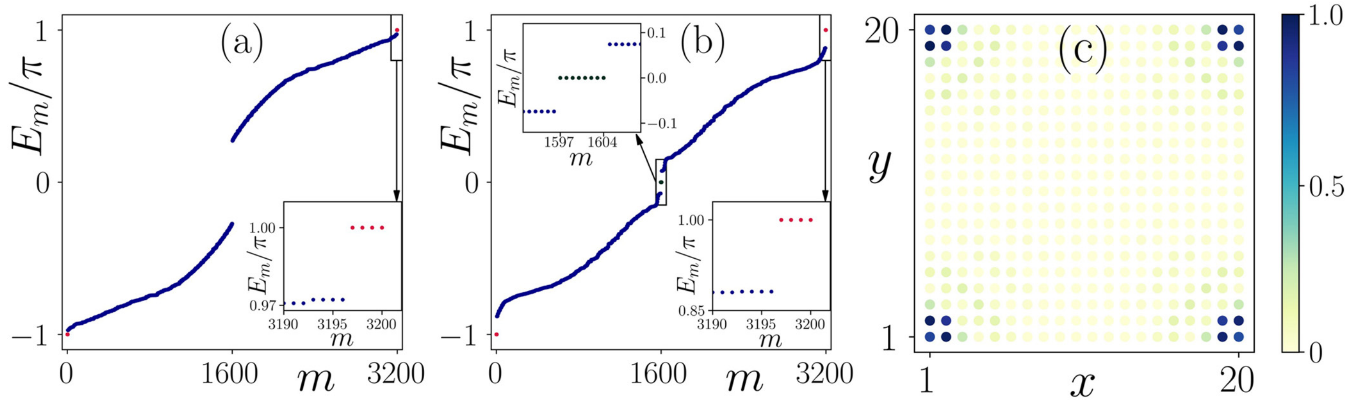

FIG. 2. We depict the quasienergy spectra as function of the state index m for the driven system starting from the (a) nontopological regime ($m_0 = -1.0$) and (b) topological regime ($m_0 = 1.0$). The 0- and π-Majorana corner modes (MCMs) are highlighted by dark-green and red dots, respectively. (c) The local density of states is illustrated for 0− and π-MCMs, which are sharply localized at the corners of the system. The other model parameters are chosen as $\gamma = \lambda = \Delta = 0.2$, $V = 1.0$, and frequency $\Omega = 3.0$ and 1.5 for (a) and (b), respectively.

tain intermediate time. We can track the trails of the MCMs throughout the drive by analyzing the total density of states (TDOS) of the MCMs present in the zero and π gap. The TDOS at quasienergy ϵ can be computed as a function of t as

$$D_\epsilon(t) = \sum_m \delta[\epsilon - E_m(t)]. \tag{7}$$

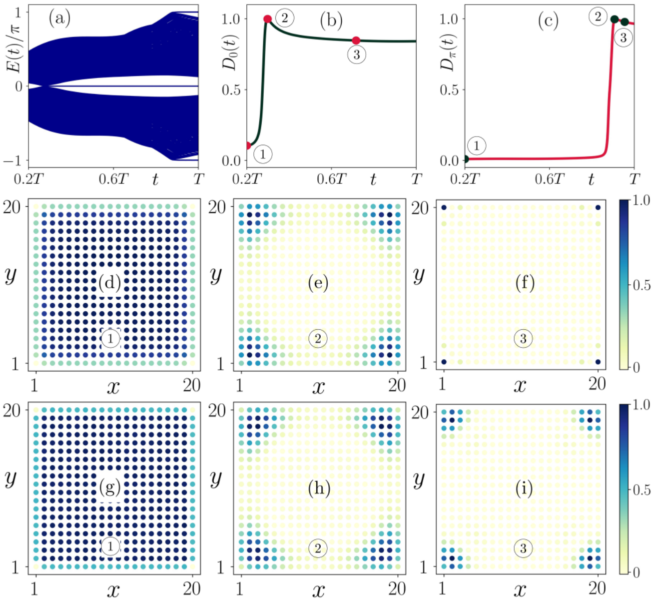

FIG. 3. (a) We demonstrate the time-dependent eigenvalue spectra $E(t)$ of the time-evolution operator $U(t, 0)$ as a function of time t during the driving period. The normalized total density of states at $E(t) = 0$ and $E(t) = \pi$ are shown with respect to time t in (b) and (c), respectively. We depict the local density of states (LDOS) at quasienergy 0 corresponding to the points marked in (b) as ① ($t = 0.84$), ② ($t = 1.25$), and ③ ($t = 3.0$), in (d), (e), and (f), respectively. In (f)–(i), we repeat (d) and (e) at quasienergy π corresponding to the designated points in (c) as ① ($t = 0.84$), ② ($t = 3.8$), and ③ ($t = 4.0$), respectively. Here, we choose the time period $T = 2\pi/\Omega \sim 4.2$ when $\Omega = 1.5$.

One can find $E_m(t)$ from the eigenvalues of $U(\mathbf{k}; t, 0)$. We illustrate $E(t)$ as a function of t in Fig. 3(a). The appearance of in-gap zero and π modes can be observed with respect to time from the eigenvalue spectra. The time evolution highlights that both the zero and π modes emerge when $t < T$ and remain there at $t = T$. However, for better identification, we show the time-dependent TDOS corresponding to quasienergy 0 and π in Figs. 3(b) and 3(c), respectively. By analyzing Figs. 3(b) and 3(c), we can reckon that both the regular 0- and π-MCMs emerge at a time $t < T$ and prevail throughout the driving period T. One can also investigate the localization properties of the 0- and π-MCMs, specifically when they start to appear. We choose three time points associated with [Figs. 3(b) and 3(c)]: ① with no 0-MCMs [π-MCMs], ② the transition point, when 0-MCMs [π-MCMs] start to appear, and ③ after generation of the 0-MCMs [π-MCMs]. We depict the LDOS at quasienergy 0 [π] corresponding to the points ①, ②, and ③ in Figs. 3(d), 3(e) and 3(f), respectively [Figs. 3(g), 3(h) and 3(i), respectively]. From Figs. 3(d) and 3(g), one can observe that no boundary modes exist when $t \ll T$, i.e., no 0-/π-MCMs are generated. At the transition point [see Figs. 3(e) and 3(h)], the zero and π modes start to populate near the corners of the system. However, we observe sharp localization near the corners of the system for zero and π modes in Figs. 3(f) and 3(g), respectively. Therefore, one can infer a connection between the time evolution of the MCMs (shown via the total density of states) to the eigenvalues of the time-evolution operator at time t as depicted via the LDOS.

IV. TOPOLOGICAL CHARACTERIZATION OF THE MCMs

We topologically characterize the regular 0- and anomalous π-MCMs employing the *dynamical nested Wilson loop technique*. The detailed discussions regarding this method can be found in Refs. [97,116]. Thus, we do not repeat the same here. To construct the dynamical second-order nested Wilson loop operator, we need the notion of a gap in which the MCMs appear. We incorporate the same via the periodized evolution operator, defined as [74,97,116]

$$U_\epsilon(\mathbf{k}; t, 0) = U(\mathbf{k}; t, 0)[U(\mathbf{k}; T, 0)]_\epsilon^{-t/T}. \tag{8}$$

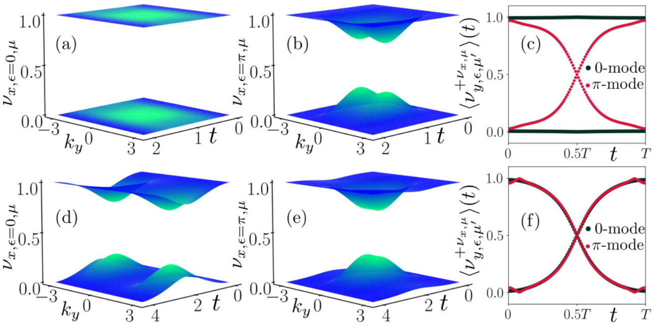

FIG. 4. We show the dynamical first-order branches $\nu_{x,\epsilon}$ in the $k_y - t$ plane for (a) zero gap and (b) π gap, corresponding to Fig. 2(a). (c) The resulting average quadrupolar motion $\langle\nu^{+\nu_{x,\epsilon}}_{y,\epsilon,\mu'}\rangle(t)$ is depicted as a function of t. The first-order branches are always gapped during the time interval $t \in [0, T]$. Since only π-Majorana corner modes (MCMs) are present in this case, $\langle\nu^{+\nu_{x,\epsilon}}_{y,\epsilon,\mu'}\rangle(t)$ crosses the 0.5 line for the π gap only. We show the dynamical first-order branches and the average quadrupolar motion, similar to (a)–(c), corresponding to the case of Fig. 2(b), in (d)–(f). Since both the 0- and π-MCMs are present in this case, $\langle\nu^{+\nu_{x,\epsilon}}_{y,\epsilon,\mu'}\rangle(t)$ crosses the 0.5 line for both of the gaps.

Here, the subscript ϵ represents the zero and π gap. We can construct $U_\epsilon(\mathbf{k}; t, 0)$ in a straightforward manner using Eq. (5). Afterward, we construct the dynamical first-order Wilson loop operator for the ϵ gap as [97,116]

$$W_{x,\epsilon,\mathbf{k}}(t) = Q_{x,\epsilon,\mathbf{k}+(L_x-1)\Delta_x\mathbf{e}_x}(t)\cdots Q_{x,\epsilon,\mathbf{k}+\Delta_x\mathbf{e}_x}(t)Q_{x,\epsilon,\mathbf{k}}(t), \tag{9}$$

where $Q_{x,\epsilon,\mathbf{k}}(t) = \frac{\mathbb{I}+U^\dagger_\epsilon(\mathbf{k}+\Delta_x\mathbf{e}_x;t,0)U_\epsilon(\mathbf{k};t,0)}{2}$, with $\Delta_x = 2\pi/L_x$ and $\mathbf{e}_x$ representing the unit vector along the x direction. The eigenvalue equation for $W_{x,\epsilon,\mathbf{k}}(t)$ can be written in the form

$$W_{x,\epsilon,\mathbf{k}}(t)\,|\nu_{x,\epsilon,\mu}(\mathbf{k},t)\rangle = e^{-2\pi i\nu_{x,\epsilon,\mu}(k_y,t)}\,|\nu_{x,\epsilon,\mu}(\mathbf{k},t)\rangle\,. \tag{10}$$

Here, $\nu_{x,\epsilon,\mu}(k_y, t)$ represents the dynamical first-order branches. We illustrate $\nu_{x,\epsilon,\mu}(k_y, t)$ in Figs. 4(a), 4(b) and 4(d), 4(e). In the former case, the system exhibits only π-MCMs, whereas the latter case supports both the 0- and π-MCMs. Interestingly, in both cases, $\nu_{x,\epsilon,\mu}(k_y, t)$ exhibit a gap throughout the driving period T and the variation of crystal momentum k_y. It therefore yields an ideal platform to construct the dynamical second-order (or nested) Wilson loop operator [97,116]. Owing to the gapped nature of the $\nu_{x,\epsilon,\mu}(k_y, t)$, one can configure two sets out of the eight $\nu_{x,\epsilon}$ such that $\nu_{x,\epsilon,\mu} \in \pm\nu_{x,\epsilon}$. We construct the dynamical nested Wilson loop operator in the subspace of $\pm\nu_{x,\epsilon}$ as

$$W^{\pm\nu_{x,\epsilon}}_{y,\epsilon,\mathbf{k}}(t) = Q^{\pm\nu_{x,\epsilon}}_{y,\epsilon,\mathbf{k}+(L_y-1)\Delta_y\mathbf{e}_y}(t)\cdots Q^{\pm\nu_{x,\epsilon}}_{y,\epsilon,\mathbf{k}+\Delta_y\mathbf{e}_y}(t)\,Q^{\pm\nu_{x,\epsilon}}_{y,\epsilon,\mathbf{k}}(t), \tag{11}$$

with $[Q^{\pm\nu_{x,\epsilon}}_{y,\epsilon,\mathbf{k}}(t)]_{\mu_1\mu_2} = \sum_{mn}[\nu_{x,\epsilon,\mu_1}(\mathbf{k}+\Delta_y\mathbf{e}_y, t)]^*_m [Q_{y,\epsilon,\mathbf{k}}(t)]_{mn}[\nu_{x,\epsilon,\mu_2}(\mathbf{k}, t)]_n$, where $Q_{y,\epsilon,\mathbf{k}}(t) = \frac{\mathbb{I}+U^\dagger_\epsilon(\mathbf{k}+\Delta_y\mathbf{e}_y;t,0)U_\epsilon(\mathbf{k};t,0)}{2}$, $\Delta_y = 2\pi/L_y$, and $\mathbf{e}_y$ is the unit vector along the y direction. We can write the eigenvalue equation for $W^{\pm\nu_{x,\epsilon}}_{y,\epsilon,\mathbf{k}}(t)$ as

$$W^{\pm\nu_{x,\epsilon}}_{y,\epsilon,\mathbf{k}}(t)\left|\nu^{\pm\nu_{x,\epsilon}}_{y,\epsilon,\mu'}(\mathbf{k},t)\right\rangle = e^{-2\pi i\nu^{\pm\nu_{x,\epsilon}}_{y,\epsilon,\mu'}(k_x,t)}\left|\nu^{\pm\nu_{x,\epsilon}}_{y,\epsilon,\mu'}(\mathbf{k},t)\right\rangle, \tag{12}$$

where $\nu^{\pm\nu_{x,\epsilon}}_{y,\epsilon,\mu'}(k_x, t)$ represents the dynamical second-order branches. Here, the k_x dependence of the $\nu^{\pm\nu_{x,\epsilon}}_{y,\epsilon,\mu'}(k_x, t)$ originates from the fact that the eigenfunctions of the dynamical first-order Wilson loop operator explicitly depend on the choice of the base point. However, its eigenvalues are independent of the specific choice of the base point. We define the average quadrupolar motion as [97,116]

$$\left\langle\nu^{+\nu_{x,\epsilon}}_{y,\epsilon,\mu'}\right\rangle(t) = \frac{1}{L_x}\sum_{k_x}\nu^{+\nu_{x,\epsilon}}_{y,\epsilon,\mu'}(k_x, t). \tag{13}$$

Note that the particles complete a round trip during the time interval $t \in [0, T]$ since $U_\epsilon(\mathbf{k}; 0, 0) = U_\epsilon(\mathbf{k}; T, 0) = \mathbb{I}$. We hence obtain two fixed points: $\langle\nu^{+\nu_{x,\epsilon}}_{y,\epsilon,\mu'}\rangle(t = 0) = \langle\nu^{+\nu_{x,\epsilon}}_{y,\epsilon,\mu'}\rangle(t = \frac{T}{2}) = 0 \pmod 1$. For a topologically trivial system, $\langle\nu^{+\nu_{x,\epsilon}}_{y,\epsilon,\mu'}\rangle(t)$ starts from 0 (mod 1) and evolves back to 0 (mod 1) during $t \in [0, T]$ and their motion can be adiabatically connected to zero when boundary is imposed [see Fig. 4(c) for zero gap]. However, if there is any obstruction due to the presence of in-gap states, i.e., the MCMs, the quadrupolar motion $\langle\nu^{+\nu_{x,\epsilon}}_{y,\epsilon,\mu'}\rangle(t \to 0) = 0$ (1) ends up at $\langle\nu^{+\nu_{x,\epsilon}}_{y,\epsilon,\mu'}\rangle(t \to T) = 1$ (0) and the two branches cross each other at 0.5 (mod 1) [see Fig. 4(c) for π gap and Fig. 4(f) for both zero and π gaps]. Such kind of motion cannot be connected to zero and thus can be utilized to distinguish between the topological and nontopological phases, in the dynamical case [97,116].

V. ANALYTICAL APPROACH: FLOQUET PERTURBATION THEORY

After investigating our setup numerically, we combine with the FPT [118–120] to achieve some analytical insights into the problem. Within the analytic scheme, we assume the amplitude of the drive V to be much larger than the hopping amplitude γ. We treat $V(t)$ [Eq. (2)] exactly and $H(\mathbf{k})$ [Eq. (1)] as a perturbation. The time-evolution operator for

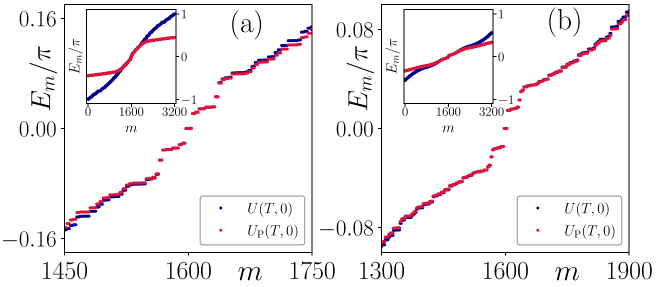

FIG. 5. We depict the quasienergy spectra (employing open boundary condition) corresponding to the exact Floquet operator $U(T, 0)$ (blue dots) and compare it with that of the perturbative Floquet operator $U_{\mathrm{P}}(T, 0)$ (red dots) for the few low-lying states for (a) $\Omega = 1.5$ and (b) $\Omega = 5.0$. We show the corresponding full quasienergy spectra in the insets of the figures. We choose $V = 10.0$ and $m_0 = 0.2$, while all the other model parameters are chosen to be of the same value as in Fig. 2.

$V(t)$ reads as

$$U_0(t,0)=\exp\left[-i\int_0^t dt' V(t')\right]=\exp\left[-\frac{iV}{\Omega}\sin(\Omega t)\,\Gamma_3\right]. \tag{14}$$

We employ the interaction picture to obtain the full time-evolution operator. Following the perturbation theory [118–120], the latter can be written in the form

$$U_{\rm P}(\mathbf{k};t,0)=U_0(t,0)\,U_{\rm I}(\mathbf{k};t,0), \tag{15}$$

where the time-evolution operator in the interaction picture $U_{\rm I}(\mathbf{k};t,0)$ can be written in the form of a power series as [118–120]

$$\begin{aligned}U_{\rm I}(\mathbf{k};t,0)&=\mathbb{I}+(-i)\int_0^t dt' H_{\rm I}(\mathbf{k},t')\\&\quad+(-i)^2\int_0^t dt_1 H_{\rm I}(\mathbf{k},t_1)\int_0^{t_1} dt_2 H_{\rm I}(\mathbf{k},t_2)+\cdots\\&=\mathbb{I}+U_{\rm I}^{(1)}(\mathbf{k};t,0)+U_{\rm I}^{(2)}(\mathbf{k};t,0)+\cdots,\end{aligned} \tag{16}$$

where $H_{\rm I}(\mathbf{k},t)=U_0(0,t)H(\mathbf{k})U_0(t,0)$. Within our analysis, we truncate the series after the first-order term in $U_{\rm I}(\mathbf{k};t,0)$ as the higher-order terms become messy large expressions with smaller magnitude. Following the periodic cosine drive [Eq. (2)], we obtain the first-order term $U_{\rm I}(t,0)$ in the perturbation series [Eq. (16)] as

$$\begin{aligned}U_{\rm I}^{(1)}(\mathbf{k};t,0)=-\frac{i}{2}\Bigg[&\left\{t+t\mathcal{J}_0(\phi)+2\sum_{n=1}^{\infty}\mathcal{J}_{2n}(\phi)\frac{\sin 2n\Omega t}{2n\Omega}\right\}H(\mathbf{k})+2i\sum_{n=1}^{\infty}\frac{\mathcal{J}_{2n-1}(\phi)}{(2n-1)\Omega}\{1-\cos[(2n-1)\Omega t]\}[\Gamma_3,H(\mathbf{k})]\\&+\left\{t-t\mathcal{J}_0(\phi)+2\sum_{n=1}^{\infty}\mathcal{J}_{2n}(\phi)\frac{\sin 2n\Omega t}{2n\Omega}\right\}\Gamma_3 H(\mathbf{k})\Gamma_3\Bigg],\end{aligned} \tag{17}$$

where $\phi=\frac{2V}{\Omega}$ and $\mathcal{J}_n$ is the Bessel function of the first kind. However, $U_{\rm P}(\mathbf{k};t,0)$ does not satisfy the unitarity condition. It is possible to recast the same at $t=T$ by exponentiating $U_{\rm I}(\mathbf{k};t,0)$ and exploiting $U_0(t,0)=\mathbb{I}$. Due to the loss of unitarity condition, $U_{\rm P}(\mathbf{k};t,0)$ does not facilitate the calculation of the average quadrupolar motion [Eq. (13)]. Following the first-order term in $U_{\rm I}(\mathbf{k};t,0)$ [Eq. (17)] and combining this with $U_0(t,0)$, the effective Hamiltonian can be computed at $t=T$ from $U_{\rm P}(\mathbf{k};T,0)$ [Eq. (15)]. The effective Hamiltonian can be obtained from the relation $U_{\rm P}(\mathbf{k};T,0)=\exp[-iH_{\rm eff}(\mathbf{k})T]$ as

$$H_{\rm eff}(\mathbf{k})=\mathcal{J}_0(\phi)[H(\mathbf{k})-\epsilon(\mathbf{k})]+\epsilon(\mathbf{k})\Gamma_3. \tag{18}$$

It is evident from the $H_{\rm eff}(\mathbf{k})$ that only the SOC and the d-wave pairing term get modulated by the drive, whereas the hopping, as well as the crystal field splitting term m_0, is unaffected by the application of the drive. The bulk gap $\Delta G(T)$, obtained from $H_{\rm eff}(\mathbf{k})$, at $\mathbf{k}=(0,0)$ and (π,π) remains unaltered as compared to the static band gap obtained from $H(\mathbf{k})$. However, the instantaneous bulk gap $\Delta G(t)$ as a function of time $t(\neq T)$ can be modulated with respect to the static band gap due to the presence of other time-dependent nonvanishing terms in Eq. (17) [see Figs. 6(a)–6(d)].

In Fig. 5, we depict the quasienergy spectra (under OBCs) for the Floquet operator constructed using Eq. (15) by substituting $t=T$. This is represented by red dots in Fig. 5. We further compare the same with that of the exact Floquet operator $U(T,0)$ (indicated by blue dots in Fig. 5). For a fixed value of V ($\gg\gamma$), we consider two cases for the driving frequency $\Omega=1.5$ and $\Omega=5.0$ as demonstrated in Figs. 5(a) and 5(b), respectively. The quasienergy spectra of the $U_{\rm P}(T,0)$ (obtained from FPT) match well with the low-lying eigenvalues $E_m\to 0$ of the exact Floquet operator $U(T,0)$. However, from the insets of Figs. 5(a) and 5(b), one can notice that the full eigenvalue spectra of $U_{\rm P}(T,0)$ do not fully match with that of $U(T,0)$. Nevertheless, it is evident from Fig. 5(b) that the overlap between the exact quasienergy (numerical) and the perturbative quasienergy (analytical) becomes more prominent as $\Omega=5.0$. The same is not true in Fig. 5(a)

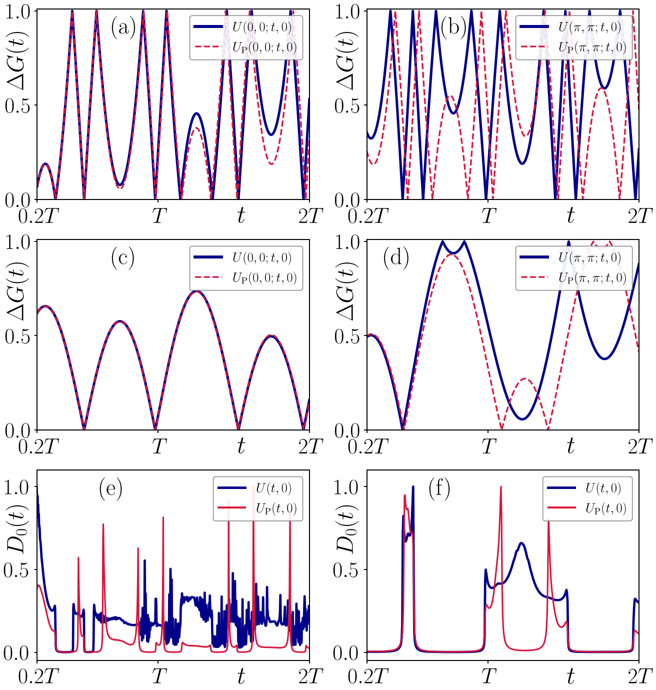

FIG. 6. We depict the bulk gap $\Delta G(t)$ as a function of t at $\mathbf{k}=(0,0)$ obtained from the exact Floquet operator $U(\mathbf{k};t,0)$ (solid blue line) and the perturbative Floquet operator $U_{\rm P}(\mathbf{k};t,0)$ (dashed red line) for (a) $\Omega=1.5$ and (c) $\Omega=5.0$. We show the same at $\mathbf{k}=(\pi,\pi)$ in (b) and (d), respectively. We illustrate the total density of states $D_0(t)$ as function of t corresponding to $\Omega=1.5$ and $\Omega=5.0$ in (e) and (f), respectively. Here, blue and red lines represent the total density of states $D_0(t)$ computed from $U(t,0)$ and $U_{\rm P}(t,0)$, respectively. We choose $V=10.0$ and $m_0=0.2$, while all other model parameters take the same value as in Fig. 2.

as $\Omega = 1.5$ is comparable with the bandwidth. Interestingly, $U_{\rm P}(T, 0)$ can capture the 0-MCMs accurately in its eigenvalue spectra. However, $U_{\rm P}(T, 0)$ fails to encapsulate the anomalous π modes.

Having investigated the quasienergy spectra, obtained employing OBCs and depicted in Fig. 5, we tend towards the time dynamics of the MCMs within the FPT scheme. First, we compare the bulk gap $\Delta G(t)$ corresponding to the quasienergy bands as a function of t around the momentum $\mathbf{k} = (0, 0)$ and $\mathbf{k} = (\pi, \pi)$, evaluated from $U_{\rm P}(\mathbf{k}; t, 0)$ and $U(\mathbf{k}; t, 0)$, in Figs. 6(a) and 6(b), respectively, for $\Omega = 1.5$. The same has been depicted in Figs. 6(c) and 6(d) choosing high frequency $\Omega = 5.0$. The bulk-gap closing points (in the time axis) at $\mathbf{k} = (0, 0)$ obtained from $U_{\rm P}(0, 0; t, 0)$ qualitatively coincide with that of $U(0, 0; t, 0)$ [see Figs. 6(a) and 6(c)]. However, at $\mathbf{k} = (\pi, \pi)$, we notice that there is a little mismatch between the gap closing points (in the time axis) obtained from $U_{\rm P}(\pi, \pi; t, 0)$ and $U(\pi, \pi; t, 0)$, i.e., the analytical and the numerical approaches. At higher frequency, the agreement between these two becomes more prominent up to the time period T, as shown in Figs. 6(b) and 6(d). Although, as we increase the time above the time period T $(t > T)$, we observe that there is a clear mismatch between the numerical and the analytical approaches even for $\Omega = 5.0$ [see Fig. 6(d)]. This mismatch remains as we increase the frequency $\Omega = 8.0$ (not shown). We believe that this mismatch occurs due to the truncation of the evolution operator $U_{\rm I}(t, 0)$ to the first-order term in the perturbation series [Eq. (16)]. By investigating the bulk-gap closing between two time intervals, we can predict the appearance or disappearance of the MCMs in the finite-size system at that said interval.

Nevertheless, we obtain a clearer picture of the time evolution of the MCMs from the investigation of the TDOS $D_0(t)$ [Eq. (7)]. We show $D_0(t)$ as a function of time t for a finite-size system in Figs. 6(e) and 6(f) for $\Omega = 1.5$ and $\Omega = 5.0$, respectively. The blue and red lines represent $D_0(t)$ calculated from $U(t, 0)$ and $U_{\rm P}(t, 0)$, respectively. For $\Omega = 1.5$, $D_0(t)$ calculated from $U_{\rm P}(t, 0)$ overlaps with that of $U(t, 0)$ only for a limited range of time. Nonetheless, both the exact and perturbative calculations suggest that the MCMs survive not only at $t = T$, but at a later time also. In the case of $\Omega = 5.0$, the $D_0(t)$ calculated using the exact and perturbative Floquet operator match substantially over the entire time window $t \in [0, 2T]$. The small mismatch accounts for the nonoverlapping of their bulk-gap closing points between $U(\pi, \pi; t, 0)$ and $U_{\rm P}(\pi, \pi; t, 0)$. Another important point to note, for $\Omega = 1.5$, is that the frequent fluctuations in the TDOS [see Fig. 6(e)] appear since the instantaneous bulk gap $\Delta G(t)$ vanishes many times in the same interval [see Figs. 6(a) and 6(b)]. However, for $\Omega = 5.0$, the number of bulk-gap vanishing points (in the time axis) is less [see Figs. 6(c) and 6(d)]. Hence, the TDOS obtained for this case is smoother in nature compared to $\Omega = 1.5$ [see Fig. 6(f)].

VI. DISCUSSIONS AND OUTLOOK

In this section, we discuss various aspects of the harmonic drive protocol and compare our FPT with the Brillouin-Wigner (BW) perturbation theory [126] that is valid in the high-frequency regime.

A. Different driving protocols

The formalism we introduced in Sec. II is not limited to the specific form of the drive [Eq. (2)]. One can introduce more sinusoidal functions in Eq. (2) and study the effect of such drives. In this regard, we propose the following driving protocols:

$$V_1(t) = V \sin(\Omega t)\Gamma_3, \tag{19a}$$

$$V_2(t) = V[\cos(\Omega t) + \sin(\Omega t)]\Gamma_3, \tag{19b}$$

$$V_3(t) = V[\cos(\Omega t) + \cos(2\Omega t) + \cos(3\Omega t)]\Gamma_3. \tag{19c}$$

Following the drive protocols mentioned in Eq. (19a)–(19c), we show the quasienergy spectra for a finite-size system in Figs. 7(a)–7(c), respectively. In all three cases, the qualitative behavior of the quasienergy spectra appears to be similar, as discussed before. The regular zero and anomalous π modes appear in all such drive protocols.

B. Recipe for generating the FSOTSC

The time-periodic harmonic drive, that we introduce in Eq. (2), cannot provide us with the 0- and/or π-MCMs for any arbitrary choices of the parameters in the Hamiltonian $H(\mathbf{k})$ [Eq. (1)]. To elaborate further, we first consider $\Delta = 0$. In this limit, one can generate the Floquet first-order TI (FFOTI), hosting zero- and π-edge modes at $E(k) = 0$ and $\pm\pi$, respectively, while examining the quasienergy spectra [82]. We depict the schematic representation of these edge modes in Figs. 8(a) and 8(c) corresponding to two cases. In case I, the counterpropagating zero- and π-edge modes intersect with each other at $k = 0, \pi$ [see Fig. 8(a)], whereas in case II, these edge modes intersect at other arbitrary momenta except $k = 0, \pi$ [see Fig. 8(c)] (here we use k to represent the quasimomentum in the slab geometry). These counterpropagating edge modes directly indicate the topological nature of the bulk gap at that quasimomentum. Therefore, the generation of the FFOTI only demands a bulk topological gap at the Floquet zone center $E(\mathbf{k}) = 0$ and/or Floquet zone boundary $E(\mathbf{k}) = \pm\pi$, irrespective of the value of the quasimomentum $\mathbf{k}$ at which the topological gap is opened. We refer to this gap as the FFOTI gap. Afterward, when we consider the harmonic drive on the underlying model with a nonzero value of Δ, these edge modes are gapped out in both of the cases I and II [see Figs. 8(b) and 8(d)]. However, only in case I, one can observe that the MCMs appear when investigated employing OBCs in both directions. By contrast, case II does not exhibit the MCMs within that bulk quasienergy gap even with $\Delta \neq 0$. The above observation signals the fact that the FFOTI gap at $\bar{\mathbf{k}} = (0, 0)$ and $\bar{\mathbf{k}} = (\pi, \pi)$ can cause the FSOTSC phase to eventually appear. On the other hand, one cannot achieve the FSOTSC phase once the FFOTI gap appears away from $\bar{\mathbf{k}} = (0, 0)$ and $\bar{\mathbf{k}} = (\pi, \pi)$. These special momentum modes are intimately related to the details of the underlying static model. The static Hamiltonian $H(\mathbf{k})$ respects the spatial symmetries $\mathrm{S} = \{\mathcal{M}_x, \mathcal{M}_y, C_4, \mathcal{M}_{xy}, \mathcal{M}_{x\bar{y}}\}$ and the corner modes are also protected by these spatial symmetries. However, only at $\bar{\mathbf{k}}(= -\bar{\mathbf{k}} \bmod 2\pi)$ does $H(\mathbf{k})$ satisfy the commutation relation: $[H(\bar{\mathbf{k}}), \mathrm{S}] = 0$. Thus, only the gap closing at $\bar{\mathbf{k}} = (0, 0)$ and $\bar{\mathbf{k}} = (\pi, \pi)$ gives rise to MCMs. Furthermore, the d-wave nature of the superconducting gap that vanishes

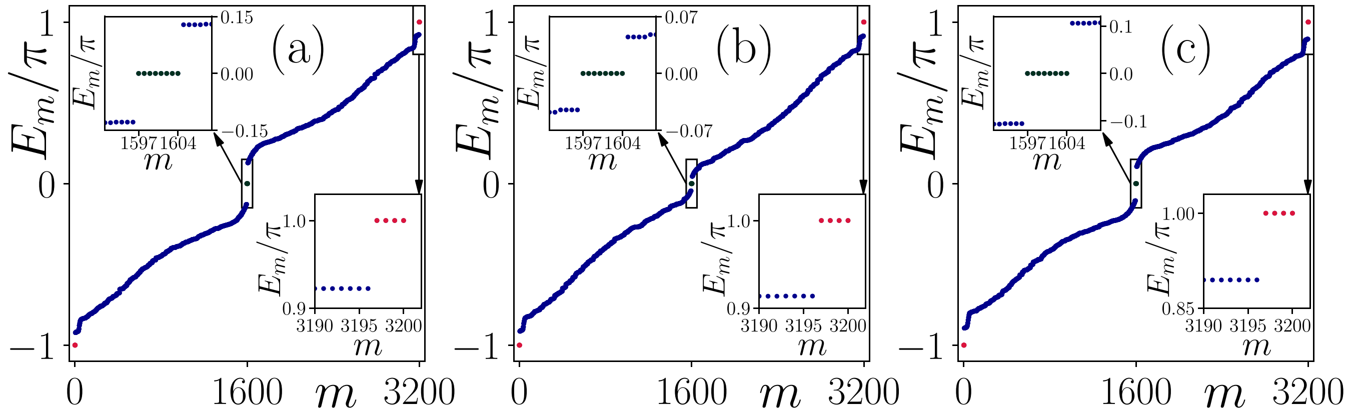

FIG. 7. In (a)–(c), we illustrate the quasienergy spectra as a function of the state index m following the drive protocols as introduced in Eqs. (19a)–(19c), respectively. We choose $\Omega = 1.5$, while all other model parameters take the same value as in Fig. 2.

at $\bar{\mathbf{k}} = (0, 0)$ and $\bar{\mathbf{k}} = (\pi, \pi)$ is also very crucial for generating the FSOTSC phase hosting 0- and π-MCMs. In short, the nature of the gap at $\bar{\mathbf{k}} = (0, 0)$ and $\bar{\mathbf{k}} = (\pi, \pi)$ in the quasienergy spectra for the FFOTI essentially determines the emergence of the FSOTSC phase, i.e., whether or not it will be observed.

Interestingly, in the step- or kick-drive protocol, one can analytically derive the Floquet operator [96,97,106,116]. Thus, a closed form of the gap closing conditions at $E(\mathbf{k}) = 0, \pi$ for $\mathbf{k} = (0, 0)/(\pi, \pi)$ can be obtained in terms of the driving parameters. However, for a periodic sinusoidal/laser irradiation, the Floquet operator $U(\mathbf{k}; T, 0)$ [Eq. (5)] cannot be cast in a closed form. Hence, the generation of 0- and π-MCMs is relatively cumbersome in the presence of such driving protocols. In particular, in case of laser irradiation drive $[\mathbf{A}(t) = A(\cos \Omega t, \sin \Omega t)]$, the quasimomenta are replaced by $\mathbf{k} \to \mathbf{k} - \mathbf{A}(t)$. Thus, finding a suitable parameter space for engineering the FSOTSC can be a formidable task and will be presented elsewhere.

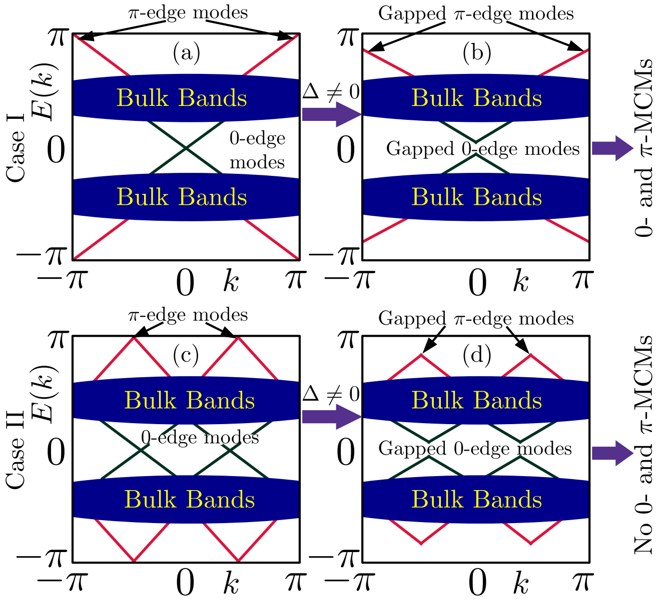

FIG. 8. We depict the schematic representation of the bulk bands and the edge modes, at $k = 0, \pm\pi$ (case I) and $k \neq 0, \pm\pi$ (case II) around $E(k) = 0$ and $E(k) = \pm\pi$ for a driven system considering slab geometry. (a) and (c) indicate that the system exhibits gapless edge states (both 0 and π) in the absence of the d-wave superconducting gap ($\Delta = 0$). These edge modes are gapped out in the presence of the superconducting term ($\Delta \neq 0$) and are shown in (b) and (d). One obtains the 0- and π-MCMs in the finite geometry under OBCs for (b), while the counterpropagating edge modes in FFOTI intersect at $k = 0, \pm\pi$. However, no 0- and π-MCMs appear for (d), while the counterpropagating edge modes in FFOTI intersect at $k \neq 0, \pm\pi$.

C. Comment on comparison between the FPT and BW perturbation theory

In the BW perturbation theory [126], one can obtain the effective Floquet Hamiltonian for a periodically driven system assuming the high-frequency limit ($\Omega \gg \gamma$). The BW effective Hamiltonian can be cast in the form [95,126]

$$H_{\rm eff}^{\rm BW}(\mathbf{k}) = H_0 + \sum_{m\neq 0} \frac{H_{-m}H_m}{m\Omega} + \mathcal{O}\left(\frac{1}{\Omega^2}\right), \tag{20}$$

where H_m's are defined in Eq. (3). In Sec. V, we study the driven system using the FPT that assumes the strength of the drive is strong, although there is no limit on the frequency of the drive in said theory. On the other hand, the BW perturbation theory contains a series of terms of the order of $1/\Omega$, and the higher-order terms in the series can be neglected in the high-frequency regime. However, with the increase in the driving amplitude, the contributions from the higher-order terms may also become more important, and curtailing the series only after the first-order term ($1/\Omega$ term) is not justified. Thus, to obtain a coherent picture from both the FPT and the BW perturbation theory, one needs to consider the higher-order terms in Eq. (20). Nevertheless, the BW perturbation theory cannot capture the anomalous π modes [126]. Hence, we do not provide the repeating results already investigated in the previous studies [95].

VII. SUMMARY AND CONCLUSIONS

To summarize, in this article, we consider a time-periodic harmonic drive protocol to generate the 2D FSOTSC anchoring both 0- and π-MCMs. We demonstrate our results for two cases. In the first case, we start from a static model which is topologically trivial, and the driven system hosts only the π-MCMs [see Fig. 2(a)]. In the second case, the starting model is topologically nontrivial and the driven system hosts both the regular 0- and anomalous π-MCMs [see Fig. 2(b)]. From the LDOS behavior, one can infer that the Majorana modes are localized at the corner of the system [see Fig. 2(c)]. Further, we study the time dynamics of the MCMs in terms of their TDOS and show that the MCMs emerge at $t < T$ and remain at $t = T$ (see Fig. 3). Also, the time dynamics of the LDOS indicates sharp localization near the corners of the system for 0- and π-MCMs when $t \sim T$. We generalize the time-dependent dynamical nested Wilson loop technique for our case following Refs. [97,116] where this has been developed for the step-drive protocol. The topological characterization of the bulk zero and π gaps is carried out with the help of the average quadrupolar motion (see Fig. 4). Moreover, we consider the strong driving amplitude limit and use the FPT to provide some analytical insights to our problem. We approximate the first-order term in the perturbation series and compare the FPT results with the exact numerical ones (see Fig. 5). The time evolution of the MCMs via the TDOS and the time-dependent quasienergy gap structure (within $t \leqslant T$) comparison indicate that the FPT yields better results in the higher-frequency regime with that of the exact ones (see Fig. 6), as far as 0-MCMs are concerned. However, the FPT is unable to capture the TDOS associated with the dynamical π-MCMs, which we leave for future studies. The disorder analog of the present problem can also lead to interesting outcomes about the stability of these modes. Also, the driving protocol and the formalism that we use in this article can be generalized to realize the three-dimensional (3D) FSOTSC hosting 1D gapless $0-/\pi$-Majorana hinge modes and 3D Floquet third-order TSC anchoring localized $0-/\pi$-MCMs.

ACKNOWLEDGMENTS

A.K.G. and A.S. acknowledge SAMKHYA: High-Performance Computing Facility provided by Institute of Physics, Bhubaneswar, for numerical computations.

---

[1] A. Y. Kitaev, Unpaired Majorana fermions in quantum wires, Phys. Usp. **44**, 131 (2001).

[2] X.-L. Qi and S.-C. Zhang, Topological insulators and superconductors, Rev. Mod. Phys. **83**, 1057 (2011).

[3] J. Alicea, New directions in the pursuit of Majorana fermions in solid state systems, Rep. Prog. Phys. **75**, 076501 (2012).

[4] J. D. Sau, R. M. Lutchyn, S. Tewari, and S. Das Sarma, Generic New Platform for Topological Quantum Computation Using Semiconductor Heterostructures, Phys. Rev. Lett. **104**, 040502 (2010).

[5] R. M. Lutchyn, J. D. Sau, and S. Das Sarma, Majorana Fermions and a Topological Phase Transition in Semiconductor-Superconductor Heterostructures, Phys. Rev. Lett. **105**, 077001 (2010).

[6] A. Haim, E. Berg, F. von Oppen, and Y. Oreg, Signatures of Majorana Zero Modes in Spin-Resolved Current Correlations, Phys. Rev. Lett. **114**, 166406 (2015).

[7] D. A. Ivanov, Non-Abelian Statistics of Half-Quantum Vortices in p-Wave Superconductors, Phys. Rev. Lett. **86**, 268 (2001).

[8] M. Freedman, A. Kitaev, M. Larsen, and Z. Wang, Topological quantum computation, Bull. Am. Math. Soc. **40**, 31 (2003).

[9] A. Kitaev, Fault-tolerant quantum computation by anyons, Ann. Phys. **303**, 2 (2003).

[10] C. Nayak, S. H. Simon, A. Stern, M. Freedman, and S. Das Sarma, Non-Abelian anyons and topological quantum computation, Rev. Mod. Phys. **80**, 1083 (2008).

[11] A. Das, Y. Ronen, Y. Most, Y. Oreg, M. Heiblum, and H. Shtrikman, Zero-bias peaks and splitting in an Al-InAs nanowire topological superconductor as a signature of Majorana fermions, Nat. Phys. **8**, 887 (2012).

[12] M. T. Deng, S. Vaitiekenas, E. B. Hansen, J. Danon, M. Leijnse, K. Flensberg, J. Nygård, P. Krogstrup, and C. M. Marcus, Majorana bound state in a coupled quantum-dot hybrid-nanowire system, Science **354**, 1557 (2016).

[13] V. Mourik, K. Zuo, S. M. Frolov, S. R. Plissard, E. P. A. M. Bakkers, and L. P. Kouwenhoven, Signatures of Majorana fermions in hybrid superconductor-semiconductor nanowire devices, Science **336**, 1003 (2012).

[14] F. Nichele, A. C. C. Drachmann, A. M. Whiticar, E. C. T. O'Farrell, H. J. Suominen, A. Fornieri, T. Wang, G. C. Gardner, C. Thomas, A. T. Hatke, P. Krogstrup, M. J. Manfra, K. Flensberg, and C. M. Marcus, Scaling of Majorana Zero-Bias Conductance Peaks, Phys. Rev. Lett. **119**, 136803 (2017).

[15] H. Zhang, Ö. Gül, S. Conesa-Boj, M. P. Nowak, M. Wimmer, K. Zuo, V. Mourik, F. K. de Vries, J. van Veen, M. W. A. de Moor, J. D. S. Bommer, D. J. van Woerkom, D. Car, S. R. Plissard, E. P. Bakkers, M. Quintero-Pérez, M. C. Cassidy, S. Koelling, S. Goswami, K. Watanabe *et al.*, Ballistic superconductivity in semiconductor nanowires, Nat. Commun. **8**, 16025 (2017).

[16] Q. L. He, L. Pan, A. L. Stern, E. C. Burks, X. Che, G. Yin, J. Wang, B. Lian, Q. Zhou, E. S. Choi, K. Murata, X. Kou, Z. Chen, T. Nie, Q. Shao, Y. Fan, S.-C. Zhang, K. Liu, J. Xia, and K. L. Wang, Chiral Majorana fermion modes in a quantum anomalous Hall insulator–superconductor structure, Science **357**, 294 (2017).

[17] A. Grivnin, E. Bor, M. Heiblum, Y. Oreg, and H. Shtrikman, Concomitant opening of a bulk-gap with an emerging possible Majorana zero mode, Nat. Commun. **10**, 1940 (2019).

[18] J. Chen, B. D. Woods, P. Yu, M. Hocevar, D. Car, S. R. Plissard, E. P. A. M. Bakkers, T. D. Stanescu, and S. M. Frolov, Ubiquitous Non-Majorana Zero-Bias Conductance Peaks in Nanowire Devices, Phys. Rev. Lett. **123**, 107703 (2019).

[19] W. A. Benalcazar, B. A. Bernevig, and T. L. Hughes, Quantized electric multipole insulators, Science **357**, 61 (2017).

[20] W. A. Benalcazar, B. A. Bernevig, and T. L. Hughes, Electric multipole moments, topological multipole moment pumping,

and chiral hinge states in crystalline insulators, Phys. Rev. B **96**, 245115 (2017).

[21] Z. Song, Z. Fang, and C. Fang, $(d-2)$-Dimensional Edge States of Rotation Symmetry Protected Topological States, Phys. Rev. Lett. **119**, 246402 (2017).

[22] J. Langbehn, Y. Peng, L. Trifunovic, F. von Oppen, and P. W. Brouwer, Reflection-Symmetric Second-Order Topological Insulators and Superconductors, Phys. Rev. Lett. **119**, 246401 (2017).

[23] F. Schindler, A. M. Cook, M. G. Vergniory, Z. Wang, S. S. Parkin, B. A. Bernevig, and T. Neupert, Higher-order topological insulators, Sci. Adv. **4**, eaat0346 (2018).

[24] S. Franca, J. van den Brink, and I. C. Fulga, An anomalous higher-order topological insulator, Phys. Rev. B **98**, 201114(R) (2018).

[25] Z. Wang, B. J. Wieder, J. Li, B. Yan, and B. A. Bernevig, Higher-Order Topology, Monopole Nodal Lines, and the Origin of Large Fermi Arcs in Transition Metal Dichalcogenides $X\mathrm{Te}_2$ ($X =$ Mo, W), Phys. Rev. Lett. **123**, 186401 (2019).

[26] M. Ezawa, Higher-Order Topological Insulators and Semimetals on the Breathing Kagome and Pyrochlore Lattices, Phys. Rev. Lett. **120**, 026801 (2018).

[27] D. Călugăru, V. Juričić, and B. Roy, Higher-order topological phases: A general principle of construction, Phys. Rev. B **99**, 041301(R) (2019).

[28] L. Trifunovic and P. W. Brouwer, Higher-Order Bulk-Boundary Correspondence for Topological Crystalline Phases, Phys. Rev. X **9**, 011012 (2019).

[29] E. Khalaf, Higher-order topological insulators and superconductors protected by inversion symmetry, Phys. Rev. B **97**, 205136 (2018).

[30] P. Szumniak, D. Loss, and J. Klinovaja, Hinge modes and surface states in second-order topological three-dimensional quantum hall systems induced by charge density modulation, Phys. Rev. B **102**, 125126 (2020).

[31] X. Ni, M. Li, M. Weiner, A. Alù, and A. B. Khanikaev, Demonstration of a quantized acoustic octupole topological insulator, Nat. Commun. **11**, 2108 (2020).

[32] B. Xie, H. Wang, X. Zhang, P. Zhan, J. Jiang, M. Lu, and Y. Chen, Higher-order band topology, Nat. Rev. Phys. **3**, 520 (2021).

[33] L. Trifunovic and P. W. Brouwer, Higher-order topological band structures, Phys. Status Solidi B **258**, 2000090 (2021).

[34] M. Geier, L. Trifunovic, M. Hoskam, and P. W. Brouwer, Second-order topological insulators and superconductors with an order-two crystalline symmetry, Phys. Rev. B **97**, 205135 (2018).

[35] X. Zhu, Tunable Majorana corner states in a two-dimensional second-order topological superconductor induced by magnetic fields, Phys. Rev. B **97**, 205134 (2018).

[36] T. Liu, J. J. He, and F. Nori, Majorana corner states in a two-dimensional magnetic topological insulator on a high-temperature superconductor, Phys. Rev. B **98**, 245413 (2018).

[37] Z. Yan, F. Song, and Z. Wang, Majorana Corner Modes in a High-Temperature Platform, Phys. Rev. Lett. **121**, 096803 (2018).

[38] Y. Wang, M. Lin, and T. L. Hughes, Weak-pairing higher order topological superconductors, Phys. Rev. B **98**, 165144 (2018).

[39] C. Zeng, T. D. Stanescu, C. Zhang, V. W. Scarola, and S. Tewari, Majorana Corner Modes with Solitons in an Attractive Hubbard-Hofstadter Model of Cold Atom Optical Lattices, Phys. Rev. Lett. **123**, 060402 (2019).

[40] R.-X. Zhang, W. S. Cole, and S. Das Sarma, Helical Hinge Majorana Modes in Iron-Based Superconductors, Phys. Rev. Lett. **122**, 187001 (2019).

[41] R.-X. Zhang, W. S. Cole, X. Wu, and S. Das Sarma, Higher-Order Topology and Nodal Topological Superconductivity in Fe(Se,Te) Heterostructures, Phys. Rev. Lett. **123**, 167001 (2019).

[42] Y. Volpez, D. Loss, and J. Klinovaja, Second-Order Topological Superconductivity in π-Junction Rashba Layers, Phys. Rev. Lett. **122**, 126402 (2019).

[43] Z. Yan, Majorana corner and hinge modes in second-order topological insulator/superconductor heterostructures, Phys. Rev. B **100**, 205406 (2019).

[44] S. A. A. Ghorashi, X. Hu, T. L. Hughes, and E. Rossi, Second-order Dirac superconductors and magnetic field induced Majorana hinge modes, Phys. Rev. B **100**, 020509(R) (2019).

[45] Sayed Ali Akbar Ghorashi, T. L. Hughes, and E. Rossi, Vortex and Surface Phase Transitions in Superconducting Higher-order Topological Insulators, Phys. Rev. Lett. **125**, 037001 (2020).

[46] Y.-J. Wu, J. Hou, Y.-M. Li, X.-W. Luo, X. Shi, and C. Zhang, In-Plane Zeeman-Field-Induced Majorana Corner and Hinge Modes in an s-Wave Superconductor Heterostructure, Phys. Rev. Lett. **124**, 227001 (2020).

[47] K. Laubscher, D. Chughtai, D. Loss, and J. Klinovaja, Kramers pairs of Majorana corner states in a topological insulator bilayer, Phys. Rev. B **102**, 195401 (2020).

[48] B. Roy, Higher-order topological superconductors in $\mathcal{P}$-, $\mathcal{T}$-odd quadrupolar Dirac materials, Phys. Rev. B **101**, 220506(R) (2020).

[49] S.-B. Zhang and B. Trauzettel, Detection of second-order topological superconductors by Josephson junctions, Phys. Rev. Res. **2**, 012018 (2020).

[50] S.-B. Zhang, W. B. Rui, A. Calzona, S.-J. Choi, A. P. Schnyder, and B. Trauzettel, Topological and holonomic quantum computation based on second-order topological superconductors, Phys. Rev. Res. **2**, 043025 (2020).

[51] S.-B. Zhang, A. Calzona, and B. Trauzettel, All-electrically tunable networks of Majorana bound states, Phys. Rev. B **102**, 100503(R) (2020).

[52] M. Kheirkhah, Z. Yan, and F. Marsiglio, Vortex-line topology in iron-based superconductors with and without second-order topology, Phys. Rev. B **103**, L140502 (2021).

[53] K. Plekhanov, N. Müller, Y. Volpez, D. M. Kennes, H. Schoeller, D. Loss, and J. Klinovaja, Quadrupole spin polarization as signature of second-order topological superconductors, Phys. Rev. B **103**, L041401 (2021).

[54] A. Tiwari, A. Jahin, and Y. Wang, Chiral Dirac superconductors: Second-order and boundary-obstructed topology, Phys. Rev. Res. **2**, 043300 (2020).

[55] Z. Yan, Higher-Order Topological Odd-Parity Superconductors, Phys. Rev. Lett. **123**, 177001 (2019).

[56] J. Ahn and B.-J. Yang, Higher-order topological superconductivity of spin-polarized fermions, Phys. Rev. Res. **2**, 012060(R) (2020).

[57] X.-J. Luo, X.-H. Pan, and X. Liu, Higher-order topological superconductors based on weak topological insulators, Phys. Rev. B **104**, 104510 (2021).

[58] Q. Wang, C.-C. Liu, Y.-M. Lu, and F. Zhang, High-Temperature Majorana Corner States, Phys. Rev. Lett. **121**, 186801 (2018).

[59] A. K. Ghosh, T. Nag, and A. Saha, Hierarchy of higher-order topological superconductors in three dimensions, Phys. Rev. B **104**, 134508 (2021).

[60] B. Roy and V. Juričić, Mixed-parity octupolar pairing and corner Majorana modes in three dimensions, Phys. Rev. B **104**, L180503 (2021).

[61] B. Fu, Z.-A. Hu, C.-A. Li, J. Li, and S.-Q. Shen, Chiral Majorana hinge modes in superconducting Dirac materials, Phys. Rev. B **103**, L180504 (2021).

[62] A. K. Ghosh and T. Nag, Non-Hermitian higher-order topological superconductors in two dimensions: Statics and dynamics, Phys. Rev. B **106**, L140303 (2022).

[63] F. Schindler, Z. Wang, M. G. Vergniory, A. M. Cook, A. Murani, S. Sengupta, A. Y. Kasumov, R. Deblock, S. Jeon, I. Drozdov *et al.*, Higher-order topology in bismuth, Nat. Phys. **14**, 918 (2018).

[64] R. Noguchi, M. Kobayashi, Z. Jiang, K. Kuroda, T. Takahashi, Z. Xu, D. Lee, M. Hirayama, M. Ochi, T. Shirasawa *et al.*, Evidence for a higher-order topological insulator in a three-dimensional material built from van der Waals stacking of bismuth-halide chains, Nat. Mater. **20**, 473 (2021).

[65] M. Serra-Garcia, V. Peri, R. Süsstrunk, O. R. Bilal, T. Larsen, L. G. Villanueva, and S. D. Huber, Observation of a phononic quadrupole topological insulator, Nature (London) **555**, 342 (2018).

[66] H. Xue, Y. Yang, F. Gao, Y. Chong, and B. Zhang, Acoustic higher-order topological insulator on a kagome lattice, Nat. Mater. **18**, 108 (2019).

[67] X. Ni, M. Weiner, A. Alu, and A. B. Khanikaev, Observation of higher-order topological acoustic states protected by generalized chiral symmetry, Nat. Mater. **18**, 113 (2019).

[68] X. Zhang, B.-Y. Xie, H.-F. Wang, X. Xu, Y. Tian, J.-H. Jiang, M.-H. Lu, and Y.-F. Chen, Dimensional hierarchy of higher-order topology in three-dimensional sonic crystals, Nat. Commun. **10**, 5331 (2019).

[69] S. Imhof, C. Berger, F. Bayer, J. Brehm, L. W. Molenkamp, T. Kiessling, F. Schindler, C. H. Lee, M. Greiter, T. Neupert *et al.*, Topoelectrical-circuit realization of topological corner modes, Nat. Phys. **14**, 925 (2018).

[70] X.-D. Chen, W.-M. Deng, F.-L. Shi, F.-L. Zhao, M. Chen, and J.-W. Dong, Direct Observation of Corner States in Second-Order Topological Photonic Crystal Slabs, Phys. Rev. Lett. **122**, 233902 (2019).

[71] B.-Y. Xie, G.-X. Su, H.-F. Wang, H. Su, X.-P. Shen, P. Zhan, M.-H. Lu, Z.-L. Wang, and Y.-F. Chen, Visualization of Higher-Order Topological Insulating Phases in Two-Dimensional Dielectric Photonic Crystals, Phys. Rev. Lett. **122**, 233903 (2019).

[72] T. Kitagawa, T. Oka, A. Brataas, L. Fu, and E. Demler, Transport properties of nonequilibrium systems under the application of light: Photoinduced quantum Hall insulators without Landau levels, Phys. Rev. B **84**, 235108 (2011).

[73] N. H. Lindner, G. Refael, and V. Galitski, Floquet topological insulator in semiconductor quantum wells, Nat. Phys. **7**, 490 (2011).

[74] M. S. Rudner, N. H. Lindner, E. Berg, and M. Levin, Anomalous Edge States and the Bulk-Edge Correspondence for Periodically Driven Two-Dimensional Systems, Phys. Rev. X **3**, 031005 (2013).

[75] G. Usaj, P. M. Perez-Piskunow, L. E. F. Foa Torres, and C. A. Balseiro, Irradiated graphene as a tunable Floquet topological insulator, Phys. Rev. B **90**, 115423 (2014).

[76] P. M. Perez-Piskunow, G. Usaj, C. A. Balseiro, and L. E. F. F. Torres, Floquet chiral edge states in graphene, Phys. Rev. B **89**, 121401(R) (2014).

[77] A. Eckardt and E. Anisimovas, High-frequency approximation for periodically driven quantum systems from a Floquet-space perspective, New J. Phys. **17**, 093039 (2015).

[78] A. Eckardt, Colloquium: Atomic quantum gases in periodically driven optical lattices, Rev. Mod. Phys. **89**, 011004 (2017).

[79] S. Yao, Z. Yan, and Z. Wang, Topological invariants of Floquet systems: General formulation, special properties, and Floquet topological defects, Phys. Rev. B **96**, 195303 (2017).

[80] T. Oka and S. Kitamura, Floquet engineering of quantum materials, Annu. Rev. Condens. Matter Phys. **10**, 387 (2019).

[81] M. Rudner and N. Lindner, Band structure engineering and nonequilibrium dynamics in Floquet topological insulators, Nat. Rev. Phys. **2**, 229 (2020).

[82] M. Umer, R. W. Bomantara, and J. Gong, Counterpropagating edge states in Floquet topological insulating phases, Phys. Rev. B **101**, 235438 (2020).

[83] T. Nag and B. Roy, Anomalous and normal dislocation modes in Floquet topological insulators, Commun. Phys. **4**, 157 (2021).

[84] Y. H. Wang, H. Steinberg, P. Jarillo-Herrero, and N. Gedik, Observation of Floquet-Bloch states on the surface of a topological insulator, Science **342**, 453 (2013).

[85] J. W. McIver, B. Schulte, F.-U. Stein, T. Matsuyama, G. Jotzu, G. Meier, and A. Cavalleri, Light-induced anomalous Hall effect in graphene, Nat. Phys. **16**, 38 (2020).

[86] Y.-G. Peng, C.-Z. Qin, D.-G. Zhao, Y.-X. Shen, X.-Y. Xu, M. Bao, H. Jia, and X.-F. Zhu, Experimental demonstration of anomalous Floquet topological insulator for sound, Nat. Commun. **7**, 13368 (2016).

[87] R. Fleury, A. B. Khanikaev, and A. Alu, Floquet topological insulators for sound, Nat. Commun. **7**, 11744 (2016).

[88] M. C. Rechtsman, J. M. Zeuner, Y. Plotnik, Y. Lumer, D. Podolsky, F. Dreisow, S. Nolte, M. Segev, and A. Szameit, Photonic Floquet topological insulators, Nature (London) **496**, 196 (2013).

[89] L. J. Maczewsky, J. M. Zeuner, S. Nolte, and A. Szameit, Observation of photonic anomalous Floquet topological insulators, Nat. Commun. **8**, 13756 (2017).

[90] R. W. Bomantara, L. Zhou, J. Pan, and J. Gong, Coupled-wire construction of static and Floquet second-order topological insulators, Phys. Rev. B **99**, 045441 (2019).

[91] T. Nag, V. Juričić, and B. Roy, Out of equilibrium higher-order topological insulator: Floquet engineering and quench dynamics, Phys. Rev. Res. **1**, 032045(R) (2019).

[92] Y. Peng and G. Refael, Floquet Second-Order Topological Insulators from Nonsymmorphic Space-Time Symmetries, Phys. Rev. Lett. **123**, 016806 (2019).

[93] R. Seshadri, A. Dutta, and D. Sen, Generating a second-order topological insulator with multiple corner states by periodic driving, Phys. Rev. B **100**, 115403 (2019).

[94] M. Rodriguez-Vega, A. Kumar, and B. Seradjeh, Higher-order Floquet topological phases with corner and bulk bound states, Phys. Rev. B **100**, 085138 (2019).

[95] A. K. Ghosh, G. C. Paul, and A. Saha, Higher order topological insulator via periodic driving, Phys. Rev. B **101**, 235403 (2020).

[96] B. Huang and W. V. Liu, Floquet Higher-Order Topological Insulators with Anomalous Dynamical Polarization, Phys. Rev. Lett. **124**, 216601 (2020).

[97] H. Hu, B. Huang, E. Zhao, and W. V. Liu, Dynamical Singularities of Floquet Higher-Order Topological Insulators, Phys. Rev. Lett. **124**, 057001 (2020).

[98] Y. Peng, Floquet higher-order topological insulators and superconductors with space-time symmetries, Phys. Rev. Res. **2**, 013124 (2020).

[99] T. Nag, V. Juričić, and B. Roy, Hierarchy of higher-order Floquet topological phases in three dimensions, Phys. Rev. B **103**, 115308 (2021).

[100] R.-X. Zhang and Z.-C. Yang, Tunable fragile topology in Floquet systems, Phys. Rev. B **103**, L121115 (2021).

[101] R. V. Bhat and S. Bera, Out of equilibrium chiral higher order topological insulator on a π-flux square lattice, J. Phys.: Condens. Matter **33**, 164005 (2021).

[102] S. Chaudhary, A. Haim, Y. Peng, and G. Refael, Phonon-induced Floquet topological phases protected by space-time symmetries, Phys. Rev. Res. **2**, 043431 (2020).

[103] W. Zhu, Y. D. Chong, and J. Gong, Floquet higher-order topological insulator in a periodically driven bipartite lattice, Phys. Rev. B **103**, L041402 (2021).

[104] J. Yu, R.-X. Zhang, and Z.-D. Song, Dynamical symmetry indicators for Floquet crystals, Nat. Commun. **12**, 5985 (2021).

[105] D. Vu, Dynamic bulk-boundary correspondence for anomalous Floquet topology, Phys. Rev. B **105**, 064304 (2022).

[106] A. K. Ghosh, T. Nag, and A. Saha, Systematic generation of the cascade of anomalous dynamical first- and higher-order modes in Floquet topological insulators, Phys. Rev. B **105**, 115418 (2022).

[107] X.-L. Du, R. Chen, R. Wang, and D.-H. Xu, Weyl nodes with higher-order topology in an optically driven nodal-line semimetal, Phys. Rev. B **105**, L081102 (2022).

[108] H. Wu, B.-Q. Wang, and J.-H. An, Floquet second-order topological insulators in non-Hermitian systems, Phys. Rev. B **103**, L041115 (2021).

[109] Z. Ning, B. Fu, D.-H. Xu, and R. Wang, Tailoring quadrupole topological insulators with periodic driving and disorder, Phys. Rev. B **105**, L201114 (2022).

[110] K. Plekhanov, M. Thakurathi, D. Loss, and J. Klinovaja, Floquet second-order topological superconductor driven via ferromagnetic resonance, Phys. Rev. Res. **1**, 032013 (2019).

[111] R. W. Bomantara and J. Gong, Measurement-only quantum computation with Floquet Majorana corner modes, Phys. Rev. B **101**, 085401 (2020).

[112] R. W. Bomantara, Time-induced second-order topological superconductors, Phys. Rev. Res. **2**, 033495 (2020).

[113] A. K. Ghosh, T. Nag, and A. Saha, Floquet generation of a second-order topological superconductor, Phys. Rev. B **103**, 045424 (2021).

[114] A. K. Ghosh, T. Nag, and A. Saha, Floquet second order topological superconductor based on unconventional pairing, Phys. Rev. B **103**, 085413 (2021).

[115] D. D. Vu, R.-X. Zhang, Z.-C. Yang, and S. Das Sarma, Superconductors with anomalous Floquet higher-order topology, Phys. Rev. B **104**, L140502 (2021).

[116] A. K. Ghosh, T. Nag, and A. Saha, Dynamical construction of quadrupolar and octupolar topological superconductors, Phys. Rev. B **105**, 155406 (2022).

[117] W. Zhu, H. Xue, J. Gong, Y. Chong, and B. Zhang, Time-periodic corner states from Floquet higher-order topology, Nat. Commun. **13**, 11 (2022).

[118] A. Sen, D. Sen, and K. Sengupta, Analytic approaches to periodically driven closed quantum systems: methods and applications, J. Phys.: Condens. Matter **33**, 443003 (2021).

[119] B. Mukherjee, A. Sen, D. Sen, and K. Sengupta, Dynamics of the vacuum state in a periodically driven Rydberg chain, Phys. Rev. B **102**, 075123 (2020).

[120] S. Ghosh, K. Saha, and K. Sengupta, Hinge-mode dynamics of periodically driven higher-order Weyl semimetals, Phys. Rev. B **105**, 224312 (2022).

[121] P. Titum, N. H. Lindner, and G. Refael, Disorder-induced transitions in resonantly driven Floquet topological insulators, Phys. Rev. B **96**, 054207 (2017).

[122] L. D'Alessio and M. Rigol, Dynamical preparation of Floquet Chern insulators, Nat. Commun. **6**, 8336 (2015).

[123] M. Suzuki, Generalized Trotter's formula and systematic approximants of exponential operators and inner derivations with applications to many-body problems, Commun. Math. Phys. **51**, 183 (1976).

[124] H. De Raedt and B. De Raedt, Applications of the generalized Trotter formula, Phys. Rev. A **28**, 3575 (1983).

[125] T. Qin, P. Zhang, and G. Yang, Nondiagonal disorder enhanced topological properties of graphene with laser irradiation, Phys. Rev. B **105**, 184203 (2022).

[126] T. Mikami, S. Kitamura, K. Yasuda, N. Tsuji, T. Oka, and H. Aoki, Brillouin-Wigner theory for high-frequency expansion in periodically driven systems: Application to Floquet topological insulators, Phys. Rev. B **93**, 144307 (2016).